micromachines

MDPI

Article

Interrogation Techniques and Interface Circuits for Coil-Coupled Passive Sensors

Marco Demori *, **Marco Baù**, **Marco Ferrari** and **Vittorio Ferrari**

Department of Information Engineering, University of Brescia, Via Branze, 38-25123 Brescia, Italy; marco.bau@unibs.it (M.B.); marco.ferrari@unibs.it (M.F.); vittorio.ferrari@unibs.it (V.F.)

* Correspondence: marco.demori@unibs.it; Tel.: +39-030-371-5897

Received: 17 August 2018; Accepted: 5 September 2018; Published: 9 September 2018

check for updates

Abstract: Coil-coupled passive sensors can be interrogated without contact, exploiting the magnetic coupling between two coils forming a telemetric proximity link. A primary coil connected to the interface circuit forms the readout unit, while a passive sensor connected to a secondary coil forms the sensor unit. This work is focused on the interrogation of sensor units based on resonance, denoted as resonant sensor units, in which the readout signals are the resonant frequency and, possibly, the quality factor. Specifically, capacitive and electromechanical piezoelectric resonator sensor units are considered. Two interrogation techniques, namely a frequency-domain technique and a time-domain technique, have been analyzed, that are theoretically independent of the coupling between the coils which, in turn, ensure that the sensor readings are not affected by the interrogation distance. However, it is shown that the unavoidable parasitic capacitance in parallel to the readout coil introduces, for both techniques, an undesired dependence of the readings on the interrogation distance. This effect is especially marked for capacitance sensor units. A compensation circuit is innovatively proposed to counteract the effects of the parasitic input capacitance, and advantageously obtain distance-independent readings in real operating conditions. Experimental tests on a coil-coupled capacitance sensor with resonance at 5.45 MHz have shown a deviation within 1.5 kHz, i.e., 300 ppm, for interrogation distances of up to 18 mm. For the same distance range, with a coil-coupled quartz crystal resonator with a mechanical resonant frequency of 4.432 MHz, variations of less than 1.8 Hz, i.e., 0.5 ppm, have been obtained.

Keywords: coil-coupled sensor; passive sensor unit; resonant sensor; telemetric sensor; distance-independent contactless interrogation

1. Introduction

The ongoing downscaling of modern sensing devices is facing the main challenges of ensuring adequate power supply sources and removing wired connections. The power supply in wireless sensors has been traditionally provided by batteries that, however, have limited lifetime and need periodic recharge/replacement. Moreover, issues related to their degradation and the environmental impact for their disposal need to be considered.

As an alternative approach, energy harvesting techniques have gained increasing interest and undergone extensive investigations. Energy is harvested from the surroundings in the form of vibrations, motion, thermal energy, or solar energy, just to name a few. Suitable energy converters have been developed to transform the harvested energy into electrical energy using different principles, like piezoelectric [1,2], electromagnetic [3], thermoelectric [4] or pyroelectric [5,6] effects. Depending on the input source, the converted power can be sufficient to supply, continuously or intermittently, one or more sensing devices, which can transmit the measurement information through a radio frequency

(RF) link to a receiving and supervising unit, thus creating a completely autonomous system without the need for power supply and cabling [7].

Alternatively, solutions based on the radio frequency identification (RFId) technologies can be adopted to implement sensing solutions exploiting electromagnetic coupling or RF fields to energize and transmit measurement information [8,9]. These solutions are typically based on low power configurations relying on a microcontroller to interface passive sensors, such as capacitive or resistive sensors [10]. Implantable sensors for medical analyses and monitoring are important examples where this solution can be advantageously applied [11–13].

Both energy harvesting and RFId systems use active electronics in the sensor unit which, in specific situations, can be a limitation, like in hostile, high-temperature, and chemically-harsh environments, where traditional silicon-based electronics cannot operate. In this context, the use of coil-coupled passive sensors, i.e., devices which do not need active components and integrated circuits to operate, is attractive. This solution exploits the magnetic coupling between a primary and a secondary coil to read passive sensors. The primary coil, along with the reading circuitry, forms the readout unit, which reads the sensor unit composed of the sensor element connected to the secondary coil [14–17]. This approach offers the promising advantage of reducing the cost of the passive sensor unit, allowing the production of disposable sensors, such as labels, with a passive sensor connected to the embedded coil [18,19].

In this paper, passive coil-coupled sensor units having a resonant behavior will be considered. The resonant behavior allows extracting the measurement information through the reading of the resonant frequency of the sensor unit [14,20]. This approach is robust because it is unaffected by the disturbances, such as noise and electromagnetic interferences, which typically affect the signal amplitude. Specifically, two kinds of sensors are investigated, as introduced in Section 2, namely, capacitive sensors, which form a resonant LC circuit with the secondary coil, and piezoelectric resonators, such as Quartz Crystal Resonators (QCRs) [21] or ceramic Resonant Piezo Layers (RPLs) [22].

One of the challenges of the contactless readout of passive sensors is to adopt reading techniques independent of the coupling between the primary and secondary coils [20,23]. This, in turn, would ensure that the readings are not affected by the interrogation distance. Two readout techniques, that are virtually independent of the coupling, are presented and discussed in detail in Section 3. In particular, a frequency-domain technique based on impedance measurements [20] and a time-domain technique called time-gated technique [21] are discussed. Both techniques suffer from significant accuracy degradation, due to the unavoidable parasitic capacitance in parallel to the readout coil that introduces a dependence of the readings on the interrogation distance. This undesirable effect is investigated in detail. Section 4 illustrates a compensation circuit that is innovatively proposed to counteract the effects of the parasitic input capacitance and advantageously obtain distance-independent readings in real operating conditions. Section 5 reports a set of experimental results on prototypes that successfully demonstrate the validity of the proposed approach and circuit.

2. Coil-Coupled Passive Sensors

A coil-coupled passive sensor is represented in its basic form by the schematic diagram of Figure 1. A primary coil CL_1 with inductance L_1 and series resistance R_1 is magnetically coupled to the secondary coil CL_2 with inductance L_2 and resistance R_2. The magnetic coupling is accounted for by the mutual inductance M, which depends on the geometry of L_1 and L_2 and their spatial arrangement. Alternatively, the magnetic coupling can be described through the coupling factor k, which is a nondimensional parameter defined as $k = M/\sqrt{(L_1 L_2)}$, resulting in $|k| \leq 1$. In the following, the values of L_1, R_1 and L_2, R_2 will be considered as fixed, while the value of M, and hence k, can change due to variations of the distance or orientation between CL_1 and CL_2.

CL_2 is connected to the generic impedance Z_S, which models the sensing element. In the following, the relevant cases will be considered where Z_S either forms, with L_2, a second order network with complex conjugate poles, i.e., Z_S is predominantly capacitive, or Z_S itself includes a second order network with complex conjugate poles, i.e., Z_S comprises an LCR network. In both cases, resonance can occur in the secondary circuit where the quantity to be sensed via Z_S influences the resonant frequency and, possibly, the damping. Therefore, the resulting combination will be termed Resonant Sensor Unit (RSU).

Importantly, for the RSU, the measurement information is carried by the frequency of the readout signal instead of its amplitude. The adoption of the resonant measuring principle has two main advantages with respect to amplitude-based techniques [24,25]. Firstly, the resonant principle is robust against external interferences or nonidealities that affect the signal amplitude. Secondly, as it will be illustrated in the following, the resonant principle, combined with suitable electronic techniques, can ensure that the readout frequency is made independent of the distance between CL_1 and the RSU.

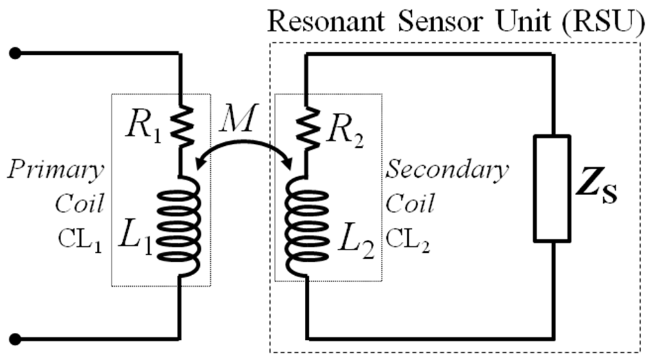

Figure 1. Equivalent circuit of a coil-coupled passive sensor.

The present theory will consider two specific cases for Z_S and the resulting RSU.

In the first case, Z_S is a capacitance sensor of value C_S, forming, with L_2, an LC resonant circuit as shown in Figure 2a. The resonant frequency f_S and quality factor Q_S of the RSU are

$$f_S = \frac{1}{2\pi\sqrt{L_2 C_S}};\ Q_S = \frac{1}{R_2}\sqrt{\frac{L_2}{C_S}}. \tag{1}$$

In the second case, Z_S is the equivalent impedance of piezoelectric resonant sensors, like QCRs and RPLs. Their electromechanical behavior around resonance can be modelled with the Butterworth–van Dyke (BVD) equivalent lumped-element circuit, as shown in Figure 2b. The BVD circuit is composed of a motional, i.e., mechanical branch, and an electrical branch. The motional branch comprises the series of inductance L_r, capacitance C_r, and resistance R_r, which respectively represent the equivalent mass, compliance, and energy losses of the resonator. The electrical branch is formed by the parallel capacitance C_0, due to the dielectric material of the resonator. Under excitation by a voltage source, the mechanical resonant frequency f_r, i.e., the frequency at which the current in the motional arm is maximum, corresponds to the series resonant frequency of the BVD circuit, i.e., the frequency at which the reactance of the mechanical branch impedance vanishes [26]. Accordingly, f_r and the quality factor Q_r of the electromechanical resonator can be expressed as

$$f_r = \frac{1}{2\pi\sqrt{L_r C_r}};\ Q_r = \frac{1}{R_r}\sqrt{\frac{L_r}{C_r}}. \tag{2}$$

Typically, when electromechanical piezoelectric resonators are used as sensors, the measurand quantity generates variations of the parameters of the motional branch L_r–C_r–R_r and, as a consequence, of f_r and Q_r.

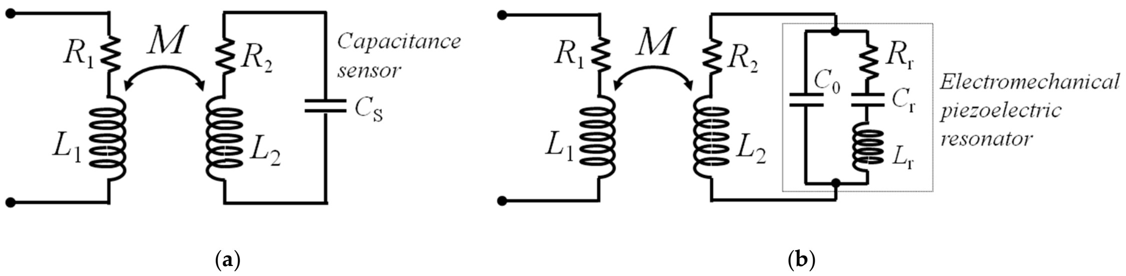

Figure 2. Equivalent circuits of the two considered cases for a coil-coupled resonant sensor unit (RSU): (**a**) capacitance sensor C_S; (**b**) electromechanical piezoelectric resonator represented with its equivalent Butterworth–van Dyke (BVD) model.

3. Analysis of the Interrogation Techniques

3.1. General Considerations

Specific interrogation techniques are required to extract information from the RSU through electronic measurements at the primary coil, exploiting the advantage of coil-coupled, i.e., contactless, operation.

One major issue to consider is the dependence of the mutual inductance M and coupling factor k of the coils on geometrical parameters, such as their distance, alignment, and relative orientation. Techniques that are influenced by the value of M, or equivalently k, would require keeping such geometrical parameters fixed and constant [27,28]. On the other hand, in most practical applications, keeping the distance and the alignment between coils fixed is unpractical/unfeasible. Therefore, as a key requirement for out-of-the-lab use of coil-coupled sensors, robust measurement techniques are demanded that are independent of k.

In the following, two innovative techniques are illustrated to perform k-independent readout of RSUs of both capacitance and electromechanical piezoelectric resonator types. In particular, the first is a frequency-domain technique which relies on the measurement of the reflected impedance at CL_1. The second is a time-domain technique, termed time-gated technique, which considers the free damped response of the RSU measured at the primary coil after that the RSU has been energized.

3.2. *k*-Independent Techniques Applied to Coil-Coupled Capacitance Sensors

Figure 3a shows the block diagram of the readout technique based on impedance measurements, where the readout system consists in an impedance analyzer connected to the primary coil CL_1. From the equivalent circuit of Figure 3b, the impedance Z_1, as a function of $\omega = 2\pi f$, is

$$Z_1 = R_1 + j\omega L_1 + Z_R = R_1 + j\omega L_1 + \omega^2 k^2 L_1 L_2 \frac{1}{R_2 + j\omega L_2 + \frac{1}{j\omega C_S}}. \tag{3}$$

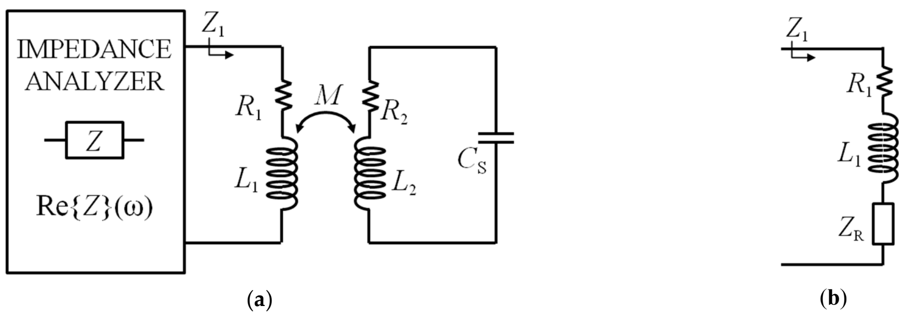

Figure 3. (**a**) Block diagram of the interrogation system based on impedance measurement from the primary coil; (**b**) equivalent circuit for the calculation of Z_1.

It can be seen from Equation (3) that the effect of the coupling with the RSU results in a reflected impedance Z_R in series with the primary coil that makes the total impedance Z_1 dependent on the coupling factor k. Nevertheless, the resonant frequency f_S and the quality factor Q_S of the RSU, defined in Equation (1), can be obtained from the real part of Z_1 [20], given by

$$\mathrm{Re}\{Z_1\}(\omega) = R_1 + \omega^2 k^2 L_1 L_2 \frac{R_2}{R_2^2 + \left(\omega L_2 - \frac{1}{\omega C_S}\right)^2}. \tag{4}$$

$\mathrm{Re}\{Z_1\}$ has a local maximum at the frequency $f_m = \omega_m/2\pi$, which can be found by equating to zero the derivative of Equation (4) with respect to ω. Interestingly enough, f_m is independent of k, and it can be related to f_S and Q_S only. Then, combining Equations (1) and (4), the following relations hold:

$$f_m = f|_{\max(\mathrm{Re}\{Z_1\})} = \frac{2Q_S}{\sqrt{4Q_S^2 - 2}} f_S;\; Q_S \approx \frac{f_S}{\Delta f_m}, \tag{5}$$

where Δf_m is the full width at half maximum (FWHM) of $\mathrm{Re}\{Z_1\}$, around f_m [20]. If Q_S is sufficiently large, then $f_m \approx f_S$, with a relative deviation $|f_m - f_S|/f_S < 100$ ppm for $Q_S > 50$. Equations (4) and (5) demonstrate that from the measurement of f_m and Δf_m in $\mathrm{Re}\{Z_1\}$, the frequency f_S and quality factor Q_S of the capacitive RSU can be advantageously extracted independently from k. Figure 4 shows sample plots of $\mathrm{Re}\{Z_1\}$ calculated for three different values of k, and illustrates the definition of Δf_m. Consistently with Equation (4), k only affects amplitude.

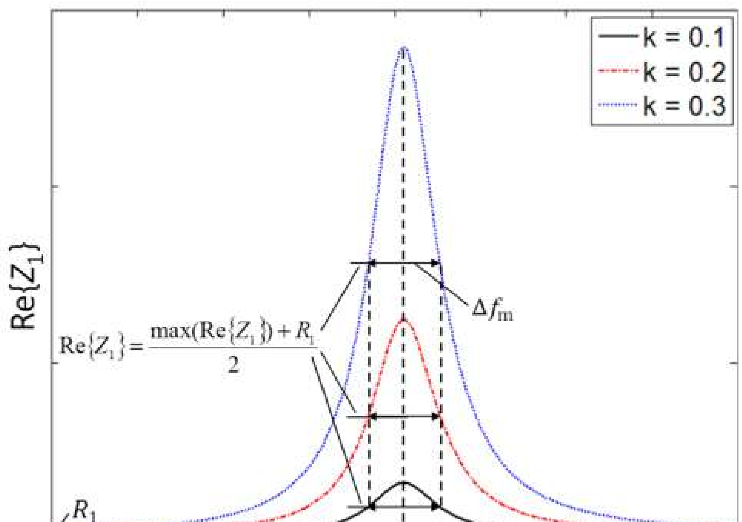

Figure 4. Real part of Z_1 as a function of frequency from Equation (4) for three different values of k.

The operating principle of the time-gated technique is shown in Figure 5a [21]. It comprises two subsequent alternating phases, namely, excitation and detection phases. During the excitation phase, when the switch is in the E position, CL_1 is connected to the sinusoidal signal $v_{exc}(t)$ to excite the RSU through inductive coupling. During the subsequent detection phase, when the switch is in the D position, the excitation signal is disconnected, and CL_1 is connected to a readout circuit with a high-impedance input, resulting in a virtually zero current in CL_1.

The input voltage $v_1(t)$ of the readout circuit during the detection phase D can be derived by taking the inverse Laplace transform of the corresponding voltage $V_1(s)$, where s is the complex frequency. Since the RSU forms a second order LCR network, the voltage $v_1(t)$ is expected to be a damped sinusoid with frequency f_d and a decay time τ_d from which the resonant frequency f_S and the quality factor Q_S of the RSU can be inferred.

Generally, assuming that the detection phase D starts at t = 0, the readout voltage $v_1(t)$ depends on the initial conditions at t = 0 of all the reactive elements, namely C_S, L_1, L_2, and M. The effect of the initial conditions on $v_1(t)$ for $t > 0$ is to globally affect only its starting amplitude, while the complex frequencies of the network, that define f_d and τ_d, are unaltered. Therefore, without losing any generality, the single initial condition V_CS0 defined as the voltage across C_S at t = 0 can be considered, neglecting the remaining ones. As an equivalent alternative that does not change the consequences of the present treatment, V_CS0 can also be seen as an effective initial condition.

As a result, the equivalent circuit of Figure 5b representing the time-gated configuration during the detection phase in the Laplace domain can be considered, and the expression of $V_1(s)$ is

$$V_1(s) = k\sqrt{\frac{L_1}{L_2}}V_\mathrm{CS0}\frac{s}{s^2 + s\frac{R_2}{L_2} + \frac{1}{L_2 C_\mathrm{S}}}. \tag{6}$$

The corresponding time expression $v_1(t)$ can be calculated:

$$v_1(t) = k\sqrt{\frac{L_1}{L_2}}\sqrt{\frac{4Q_\mathrm{s}^2}{4Q_\mathrm{s}^2 - 1}}V_\mathrm{CS0}e^{-\frac{t}{\tau_\mathrm{d}}}\cos\left[2\pi f_\mathrm{d} t - \mathrm{atan}\left(\frac{1}{2\pi f_\mathrm{d}\tau_\mathrm{d}}\right)\right]. \tag{7}$$

The signal $v_1(t)$ is a damped sinusoid with damped frequency f_d and decay time τ_d that are related to f_S and Q_S of the RSU as

$$f_\mathrm{d} = f_\mathrm{S}\sqrt{1 - \frac{1}{4{Q_\mathrm{S}}^2}};\ \tau_\mathrm{d} = \frac{Q_\mathrm{S}}{\pi f_\mathrm{S}}. \tag{8}$$

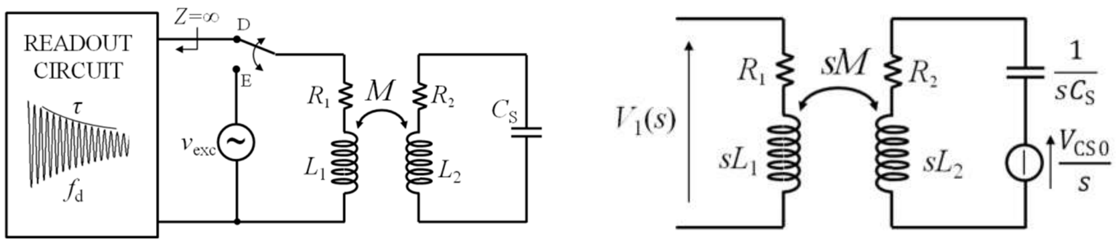

(**a**) (**b**)

Figure 5. (**a**) Block diagram of the time-gated technique; (**b**) equivalent circuit of the time-gated technique during the detection phase.

If Q_S is sufficiently large, it results in $f_\mathrm{d} \approx f_\mathrm{S}$, with a relative deviation $|f_\mathrm{d} - f_\mathrm{S}|/f_\mathrm{S} < 50$ ppm for $Q_\mathrm{S} > 50$. Notably, the coupling factor k only acts as an amplitude factor on $v_1(t)$ without influencing either f_d or τ_d. Figure 6 reports sample plots of $v_1(t)$ calculated for three different values of k.

In summary, Equations (7) and (8) demonstrate that, under the assumptions made, the time-gated technique can also allow extraction of the frequency f_S and quality factor Q_S of the capacitive RSU, independently of k.

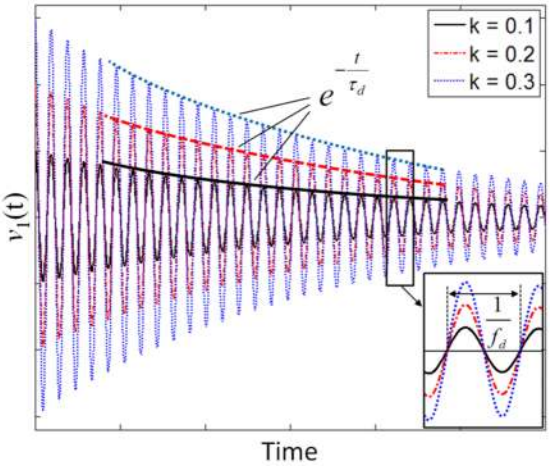

Figure 6. Voltage v_1(t) during the detection phase calculated for three different values of the coupling factor *k*.

3.3. k-Independent Techniques Applied to Coil-Coupled Electromechanical Piezoelectric Resonators

Considering the technique based on impedance measurements with reference to the equivalent circuit of Figure 2b, the impedance Z_1 measured at the primary coil can be expressed as

$$Z_1 = R_1 + j\omega L_1 + \omega^2 k^2 L_1 L_2 \frac{1}{R_2 + j\omega L_2 + \frac{1}{j\omega C_0} \Big|\Big| \left(j\omega L_r + \frac{1}{j\omega C_r} + R_r \right)}. \quad (9)$$

As it can be observed in Equation (9), the impedance Z_1 depends on the coupling factor k. Nevertheless, also in this case, the frequency f_r can be extracted from the frequency of the maximum of the real part of Z_1.

Close to the angular frequency $\omega_r = 2\pi f_r$, the impedance of the motional arm $Z_r = R_r + j\omega L_r + 1/(j\omega C_r)$ has a magnitude typically much smaller than that of the impedance of C_0, i.e., $|Z_r| << 1/\omega C_0$. Then, the presence of C_0 can be neglected, resulting in the simplified equivalent circuit of Figure 7a. Accordingly, Re{Z_1} around ω_r has the following approximated expression:

$$\mathrm{Re}\{Z_1\} \approx R_1 + \omega^2 k^2 L_1 L_2 \frac{R_r + R_2}{(R_r + R_2)^2 + \left[\omega(L_r + L_2) - \frac{1}{\omega C_r} \right]^2}. \quad (10)$$

Equation (10) has the same form as Equation (4) and, hence, Re{Z_1} has a maximum at the frequency f_{m_r} given by

$$f_{m\_r} = f_{r2} \frac{2Q_{r2}}{\sqrt{4Q_{r2}^2 - 2}}, \text{ where } f_{r2} = \frac{1}{2\pi\sqrt{(L_r + L_2)C_r}} \text{ and } Q_{r2} = \frac{1}{R_r + R_2}\sqrt{\frac{L_r + L_2}{C_r}}. \quad (11)$$

It can be observed that for large Q_{r2}, $f_{m\_r} \approx f_{r2}$ with a deviation $|f_{m\_r} - f_{r2}|/f_{r2} < 100$ ppm for $Q_{r2} > 50$. In addition, assuming that $L_2 << L_r$, the frequency f_{r2} approximates f_r and, hence, $f_{m\_r} \approx f_r$ holds. Similarly, if $R_2 << R_r$, Q_{r2} approaches Q_r. Importantly, again, the coupling factor k acts only as an amplitude factor that advantageously does not affect either the frequency or the quality factor of the resonance.

Considering, now, the frequencies $\omega >> \omega_r$, the impedance magnitude of C_0 is smaller than the impedance magnitude of Z_r, which then can be neglected, obtaining the equivalent circuit of Figure 7b. Consequently, the following approximated expression of $\mathrm{Re}\{Z_1\}$ results:

$$\mathrm{Re}\{Z_1\} \approx R_1 + \omega^2 k^2 L_1 L_2 \frac{R_2}{R_2^2 + \left(\omega L_2 - \frac{1}{\omega C_0}\right)^2}. \tag{12}$$

Also Equation (12) has the same form as Equation (4), and it can be seen that $\mathrm{Re}\{Z_1\}$ now has a maximum at the frequency $f_{\mathrm{m\_el}}$:

$$f_{\mathrm{m\_el}} = f_{\mathrm{el}} \frac{2Q_{\mathrm{el}}}{\sqrt{4Q_{\mathrm{el}}{}^2 - 2}}, \text{ where } = f_{\mathrm{el}} = \frac{1}{2\pi\sqrt{L_2 C_0}} \text{ and } Q_{\mathrm{el}} = \frac{1}{R_2}\sqrt{\frac{L_2}{C_0}}. \tag{13}$$

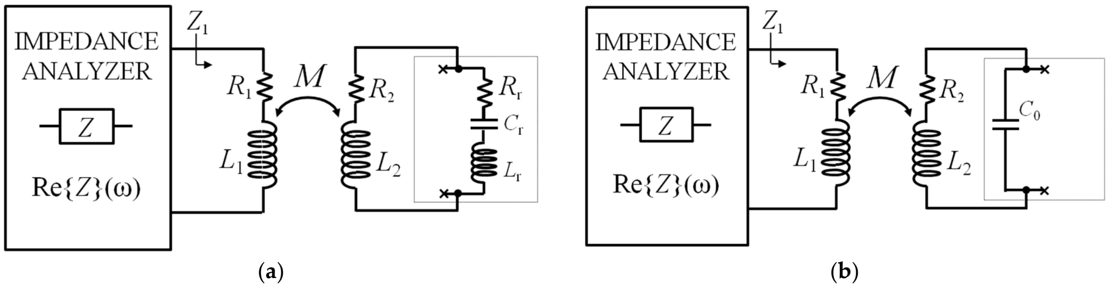

Figure 7. (**a**) Block diagram of the interrogation system with equivalent circuit of electromechanical piezoelectric resonator around f_r; (**b**) block diagram of the interrogation system with equivalent circuit of electromechanical piezoelectric resonator for $f >> f_r$.

From the previous analysis, it can be concluded that $\mathrm{Re}\{Z_1\}$ has two peaks: the first is related to the mechanical resonance f_r, the second to the electrical resonance f_{el}. With the previous assumptions on the values of L_r and L_2, and considering that, typically, $C_r << C_0$, then it follows that $f_{\mathrm{el}} >> f_r$.

To validate, numerically, the proposed approximations, Figure 8a,b report the comparison of the values of $f_{\mathrm{m\_r}}$ and $f_{\mathrm{m\_el}}$ derived respectively from Equations (11) and (13), and the frequency of the maxima derived numerically from $\mathrm{Re}\{Z_1\}$ in Equation (9) as a function of L_2. The following values of the BVD model of a 4.432 MHz AT-cut QCR have been used: C_0 = 5.72 pF, R_r = 10.09 Ω, L_r = 77.98 mH, and C_r = 16.54 fF. For CL_1 and CL_2, the values of the electrical parameters are L_1 = 8.5 μH, R_1 = 5 Ω, and R_2 = 5 Ω.

Figure 8a shows that for L_2 up to 10 μH, the values of $f_{\mathrm{m\_r}}$ predicted from Equation (11) are within 3 ppm with respect to the numerical solutions from Equation (9). Additionally, for the same range of variation of L_2, a remarkable agreement is obtained between $f_{\mathrm{m\_el}}$ predicted from Equation (13) and the numerical solution.

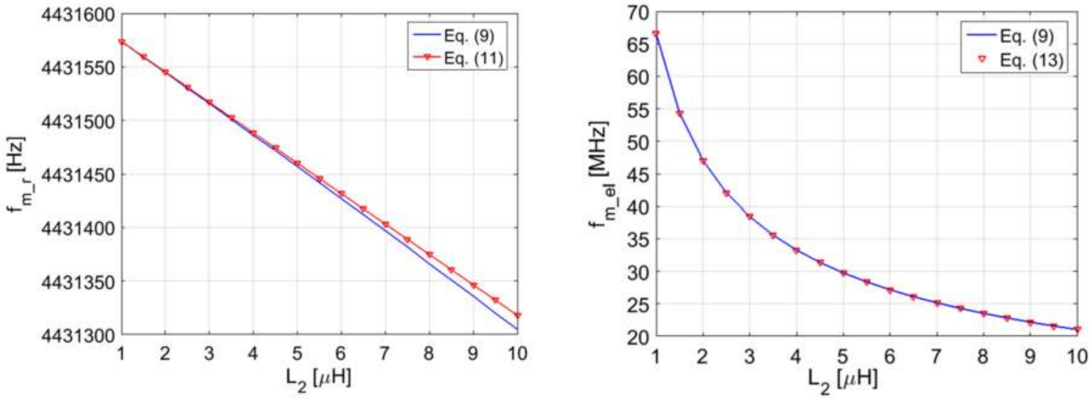

(**a**) (**b**)

Figure 8. (**a**) Comparison of $f_{\mathrm{m\_r}}$ derived from the maximum of Re{Z_1} for frequencies around f_{r}, in Equation (9), and the approximate value from Equation (11) as a function of L_2; (**b**) comparison of $f_{\mathrm{m\_el}}$ derived from the maximum of Re{Z_1} for $f >> f_{\mathrm{r}}$, in Equation (9), and the approximate value from Equation (13) as a function of L_2.

The possibility to interrogate coil-coupled electromechanical piezoelectric resonators with the time-gated technique independently from the coupling has been previously demonstrated [21].

The RSU configuration of Figure 9 has been studied in [21], showing that the open circuit voltage $v_1(t)$ at CL_1 during the detection phase, after the RSU has been energized in the excitation phase, is the sum of two damped sinusoids: one at frequency $f_{\mathrm{d\_r}}$ with exponential decaying time τ_{r}, and one at frequency $f_{\mathrm{d\_el}}$ with exponential decaying time τ_{el}.

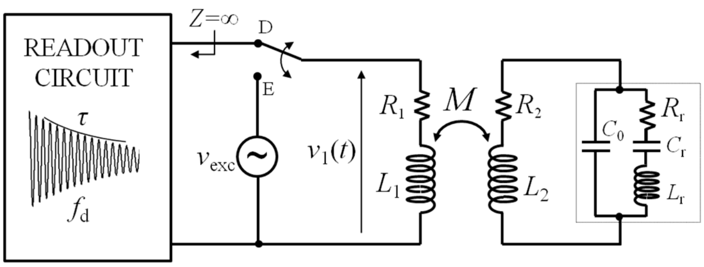

Figure 9. Block diagram of the time-gated technique applied to a coil-coupled electromechanical piezoelectric resonator.

The damped sinusoid at $f_{\mathrm{d\_r}}$ is due to the mechanical response of the resonator, while the one at $f_{\mathrm{d\_el}}$ is due to the electrical response of L_2 that interacts with the electrical capacitance C_0. In addition, for suitable values of L_2 and R_2, and considering the typical values of the equivalent parameters of the BVD model of a QCR, the decaying time τ_{r} is orders of magnitude larger than τ_{el}. Thus, the damped sinusoid at frequency $f_{\mathrm{d\_el}}$ decays to zero much faster than the damped sinusoid at frequency $f_{\mathrm{d\_r}}$. Hence, the former can be neglected in the expression of $v_1(t)$, which results in

$$v_1(t) \cong k\sqrt{L_1 L_2} A_{\mathrm{r}} e^{-\frac{t}{\tau_{\mathrm{r}}}} \cos(2\pi f_{\mathrm{d\_r}} t + \theta_{\mathrm{r}}) - \delta(t) L_1 i_{L1}(0), \tag{14}$$

where the amplitude and phase coefficients A_{r} and θ_{r} are functions of both the initial conditions at the beginning of the detection phase (t = 0), and the electrical and mechanical parameters of the system. The last term represents the contribution of the initial current $i_{L1}(0)$ in the primary inductor. From Equation (14), it can be seen that k acts only as a scaling factor for the amplitude of v_1, without affecting the sensor response parameters $f_{\mathrm{d\_r}}$ and τ_{r}. From a simplified analysis that considers the undamped system with R_2 = 0 and R_{r} = 0, under the hypothesis that $(\omega C_0)^{-1} >> \omega L_2$ at the frequency

f_r and that Q_r is large, it has been obtained that the frequency f_{d_r} can be approximated with the following relation:

$$f_{d\_r} \approx f_r\left(1 - \frac{1}{2}\frac{L_2}{L_r}\right). \tag{15}$$

It can be observed in Equation (15) that f_{d_r} depends on the ratio between L_2 and L_r. Nevertheless, if $L_2 << L_r$ the frequency f_{d_r} tends to the resonant frequency f_r of the electromechanical resonator. A numerical analysis that allows the calculation of the parameters f_{d_r} and τ_r of the complete system, is also reported in [21]. The results can be directly compared with Figure 8, the values of the parameters of the BVD model used in the numerical analysis being the same. Also in that case, good agreement between the values of f_{d_r} predicted from Equation (15) and the numerical results have been obtained, with a maximum deviation within 3 ppm for L_2 up to 10 µH.

3.4. Effect of Parasitic Capacitance at the Primary Coil on Coil-Coupled Capacitance Sensors

When the proposed techniques are transferred into real electronic circuits, unavoidable nonidealities result in a lumped parasitic capacitance C_P that appears in parallel to L_1. The parasitic capacitance C_P is mainly composed of the parasitic capacitance of the inductor L_1, the capacitance of the connections, and the input capacitance of the electronic interface.

The effect of C_P is now evaluated, firstly, considering the case of the RSU with the capacitance sensor, extending the treatment of Section 3.2.

With reference to Figure 10a, the real part of the impedance at the primary coil becomes

$$\mathrm{Re}\{Z_{1P}\} = \mathrm{Re}\left\{\frac{\left(R_1 + j\omega L_1 + \frac{\omega^2 k^2 L_1 L_2}{R_2 + j\omega L_2 + \frac{1}{j\omega C_S}}\right)\frac{1}{j\omega C_P}}{R_1 + j\omega L_1 + \frac{\omega^2 k^2 L_1 L_2}{R_2 + j\omega L_2 + \frac{1}{j\omega C_S}} + \frac{1}{j\omega C_P}}\right\}. \tag{16}$$

As discussed in [23], with $C_P \neq 0$, Equation (16) no longer allows extraction of f_S and Q_S independently from the coupling factor k, which now is in the expression of Z_{1P} and affects Re{Z_{1P}}, not only as a scaling factor. In particular, it has been shown by a numerical analysis of Equation (16) that Re{Z_{1P}} has two maxima, corresponding, respectively, to a primary resonance near f_S and a secondary resonance near $f_P = 1/\left(2\pi\sqrt{L_1 C_P}\right)$. Both the frequencies of the maxima and the trend of Re{Z_{1P}} are influenced by the coupling factor k [23].

Considering now the time-gated technique, the voltage $v_{1P}(t)$ at the primary coil in the detection phase can be obtained from the circuit of Figure 10b. Adopting the same approach as for the case of C_P = 0, it will be assumed that all the reactive elements, except the capacitor C_S, have zero initial conditions at t = 0. Consequently, the voltage $V_{1P}(s)$ can be expressed in the Laplace domain as

$$V_{1P}(s) = \frac{N(s)}{D(s)} = k\sqrt{\frac{L_1}{L_2}}\frac{sV_{CS0}C_S L_2}{s^4 C_S C_P L_1 L_2(1-k^2) + s^3 C_S C_P(L_1 R_2 + L_2 R_1) + s^2(C_S L_2 + C_P L_1 + C_S C_P R_1 R_2) + s(C_S R_2 + C_P R_1) + 1}, \tag{17}$$

where V_{CS0} is the voltage across C_S at t = 0. From Equation (17), it can be seen that k, besides acting as a scaling factor, also features in the coefficient of fourth degree in the polynomial $D(s)$. Consequently, it is expected that the complex frequencies are dependent on k. Taking the inverse Laplace transform of Equation (17), it results that the expression of $v_{1P}(t)$ is composed of the sum of two damped sinusoids as

$$v_{1P}(t) = A_1 e^{-\frac{t}{\tau_{d1}}}\cos(2\pi f_{d1} t - \theta_1) + A_2 e^{-\frac{t}{\tau_{d2}}}\cos(2\pi f_{d2} t - \theta_2), \tag{18}$$

where A_1 and A_2 are amplitude coefficients and θ_1 and θ_2 are phase angles that depend on the parameters of the circuit and the initial conditions. The frequencies f_{d1} and f_{d2} and the decay times, τ_{d1} and τ_{d2} are obtained by the complex conjugate solutions $p_{1,2} = 1/\tau_{d1} \pm j2\pi f_{d1}$ and $p_{3,4} = 1/\tau_{d2} \pm j2\pi f_{d2}$ of $D(s) = 0$.

From the values of $p_{1,2}$ and $p_{3,4}$, it can be demonstrated that f_{d1} is close to f_P, while f_{d2} is close to f_S, but both f_{d1} and f_{d2} are dependent on k. For R_2 sufficiently smaller than R_1, a decay time τ_{d2} larger than τ_{d1} can be obtained. In this condition, in $v_{1P}(t)$ the damped sinusoid at f_{d1} falls off more rapidly than that at f_{d2}, and it becomes negligible as time elapses. Importantly, since f_{d2} depends on k, the distance-independent operation of the case $C_P = 0$ is now lost.

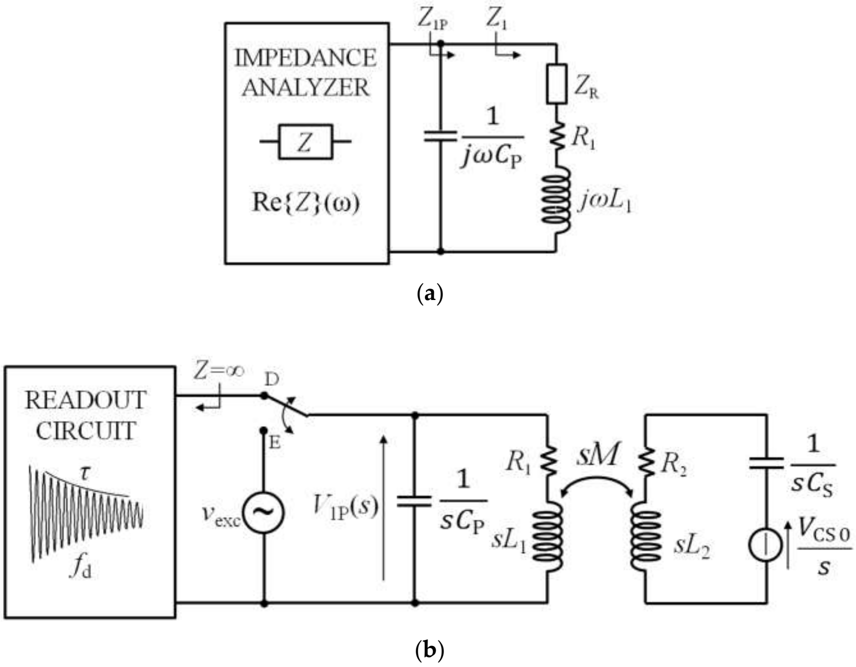

Figure 10. (**a**) Block diagram of the interrogation system with equivalent circuit of the impedance Z_{1P} for the technique based on impedance measurements applied to a coil-coupled capacitance sensor; (**b**) block diagram of the interrogation system with equivalent circuit in the Laplace domain to derive $V_{P1}(s)$ during the detection phase of the time-gated technique applied to a coil-coupled capacitance sensor.

The dependence of the readout frequency on the coupling factor k, introduced by the parasitic capacitance C_P, on both the proposed techniques, is investigated by numerical analysis. For the RSU and CL_1, the following sample values, which represent real conditions well, have been considered: L_2 = 8 μH, C_S = 100 pF, R_2 = 3 Ω, $L_1 = L_2$, and R_1 = 10 Ω. For the impedance technique, the frequency f_{SP} has been calculated from the expression of Re{Z_{1P}}, adopting the definitions in Equation (5). For the time-gated technique, f_{SP} has been calculated from f_{d2} and τ_{d2}, derived from the numerical solution of $D(s) = 0$, adopting the definitions in Equation (8).

Figure 11 compares the obtained relative deviation $(f_{SP} - f_S)/f_S$ as a function of the coupling factor k for three different values of C_P/C_S. For the considered values of the parameters, C_P ranges from 1 pF to 10 pF. As it can be observed, $(f_{SP} - f_S)/f_S$ deviates from zero, corresponding to $C_P = 0$. The deviation increases for increasing k of an amount that augments with C_P/C_S. Noticeably, both the techniques are equally affected by the inaccuracies introduced by C_P, in terms of the dependence of the readout frequency on k. These results demonstrate that C_P prevents accurate distance-independent measurements from being obtained.

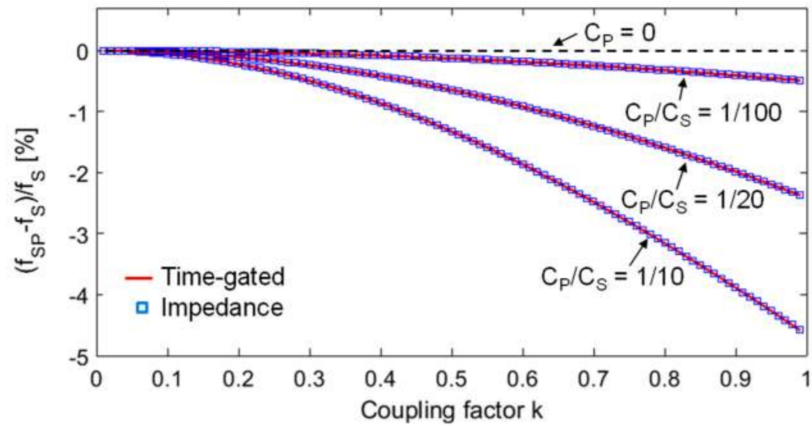

Figure 11. Comparison of the $(f_{SP} - f_S)/f_S$ obtained from the two techniques as a function of k for three different values of the ratio C_P/C_S. The exact value of f_S without the parasitic capacitance, i.e., C_P = 0, is f_S = 5.626977 MHz.

3.5. Effect of Parasitic Capacitance at the Primary Coil on Coil-Coupled Electromechanical Piezoelectric Resonators

Considering, now, the case with coil-coupled electromechanical piezoelectric resonators, the dependence on k due to C_P can be evaluated by using the same numerical approach as discussed in Section 3.3. The resonant frequency f_{rP} can be obtained from numerical analysis of the equivalent circuit in Figure 12a for the frequency-domain technique based on impedance Z_{1P}, while the equivalent circuit of Figure 12b must be considered for the time-gated technique to determine $V_{1P}(s)$.

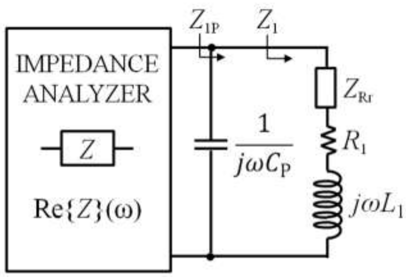

(**a**)

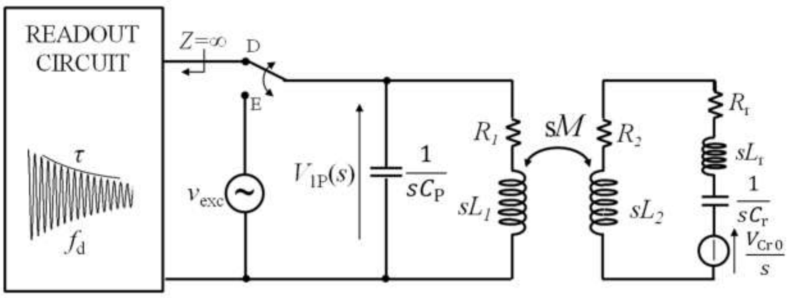

(**b**)

Figure 12. (**a**) Block diagram of the interrogation system with equivalent circuit of the impedance Z_{1P} for the technique based on impedance measurements applied to an electromechanical piezoelectric resonator; Z_{Rr} represents the reflected impedance of the RSU with electromechanical piezoelectric resonator. (**b**) Block diagram of the interrogation system with equivalent circuit in the Laplace domain to derive $V_{1P}(s)$ during the detection phase of the time-gated technique applied to an electromechanical piezoelectric resonator.

In both the equivalent circuits, the impedance of the static capacitance C_0 has been considered high enough to be neglected. For the time-gated technique, C_P is expected to give rise to an additional damped sinusoid in $v_{1P}(t)$, with a damped frequency related to C_P resonating with L_1. However, the numerical simulations have demonstrated that this sinusoid fades out more quickly than the damped sinusoid, due to the QCR response.

Considering the same parameter values for the QCR as adopted for the analysis of Figure 8, the obtained relative deviation $(f_{rP} - f_r)/f_r$ as a function of k for three different increasing values of the ratio C_P/C_r, is reported in Figure 13. For the considered values of the parameters, C_P ranges from 1.65 pF to 99.2 pF. The baseline, i.e., the dotted curve corresponding to $C_P = 0$, is at -54.5 ppm because of L_2, that slightly affects f_{r2} and, hence, f_{rP}, according to Equation (11). As it can be observed, f_{rP} has a maximum variation of less than 4 ppm with respect to the baseline. Remarkably, also in this case, the same behaviour with respect to C_P and k is predicted for the two techniques.

The quantitatively negligible dependence of f_{rP} on k can be ascribed to the fact that the inductive component in the RSU is dominated by L_r. In fact, L_r is three orders of magnitude larger than L_2, and it is not involved in the coupling between the primary coil and the RSU. This result shows that with coil-coupled electromechanical resonators, such as QCRs, the proposed techniques remain practically independent from the coupling factor k, despite a not-negligible C_P.

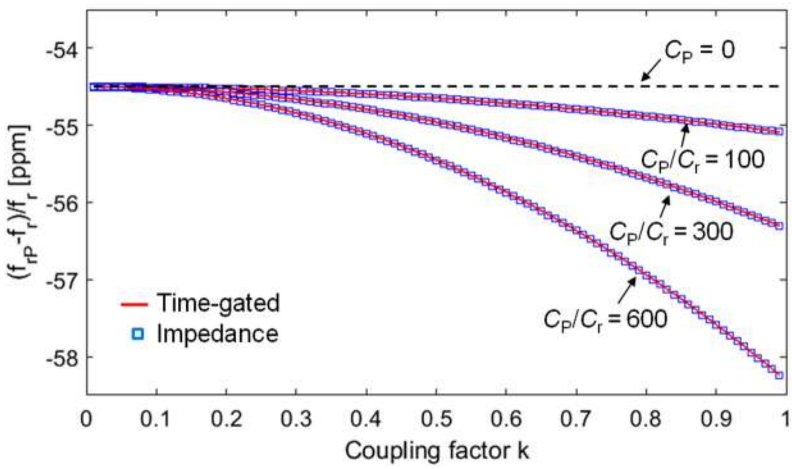

Figure 13. Comparison of the relative deviation $(f_{rP} - f_r)/f_r$ obtained from the time-gated technique and the impedance technique as a function of k for three different values of the ratio C_P/C_r.

4. Interrogation Techniques and Interface Circuits

4.1. Interrogation System Based on the Impedance-Measurement Technique with Parasitic Capacitance Compensation

The block diagram of the interrogation system, based on impedance-measurement technique, is reported in Figure 14. The primary coil CL_1 is connected to the impedance analyzer. The total parasitic capacitance C_P accounts for the contributions given by the parasitic capacitances of CL_1, the connections and the equivalent capacitance of the input of the impedance analyzer, represented in Figure 14 with C_1, C_L, and C_I, respectively.

The key idea is that connecting a proper capacitance compensation circuit to the primary coil CL_1, it is possible to cancel the effects of C_P. The proposed compensation circuit, described in Section 4.3, behaves as an equivalent negative capacitance $-C_C$. The ideal condition, where C_P is not present, i.e., $Z_{1P} = Z_1$, can be thus obtained when $C_C = C_P$. In the compensated condition, Equation (5) again applies, and k-independent measurements of the resonant frequency and quality factor can be obtained by considering the maximum of the real part of the measured impedance.

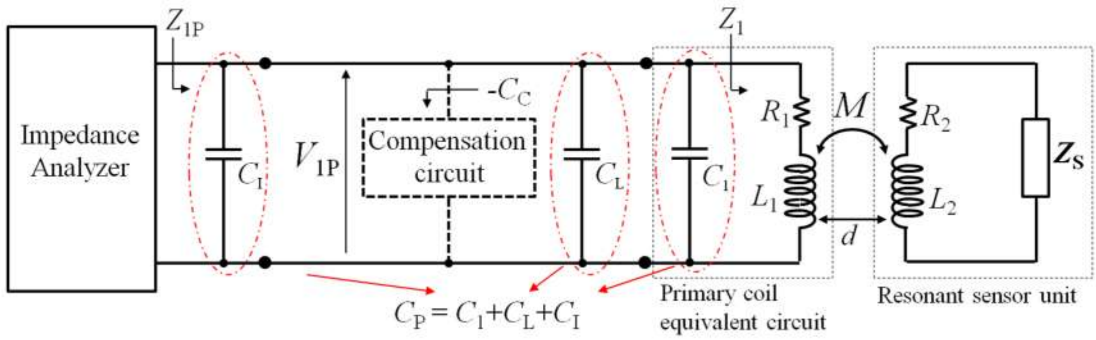

Figure 14. Block diagram of the interrogation system based on impedance measurement technique with parasitic capacitance compensation circuit.

4.2. Interrogation System Based on the Time-gated Technique with Parasitic Capacitance Compensation

The block diagram of the proposed interrogation system based on the time-gated technique is shown in Figure 15. The analog switch SW, controlled by the square-wave gate signal $v_g(t)$, alternatively connects the primary coil to the excitation signal $v_{exc}(t)$ and to the high-input impedance readout amplifier A_G during the excitation and detection phases, respectively. The noninverting amplifier A_G, with gain G, is based on a high-bandwidth operational amplifier. A frequency meter connected to the output of A_G allows measurement of the frequency of the damped sinusoidal signal $v_O(t)$.

The total parasitic capacitance C_P accounts for the contributions of the parasitic capacitances of the primary coil, the connections, the analog switch SW, and the equivalent input capacitance of the amplifier A_G, represented in Figure 15 with C_1, C_L, C_{SW}, and C_I, respectively.

Similarly to what was described in Section 4.1, a proper compensation circuit that behaves as an equivalent negative capacitance $-C_C$ can be introduced to cancel C_P. In the compensated condition, the frequency and decay time of the damped sinusoidal voltage $v_O(t)$ return to be unaffected from the coupling factor k. In this condition, Equation (8) can be used to extract the resonant frequency and quality factor of the RSU from the measured resonant frequency and decay time of $v_O(t)$.

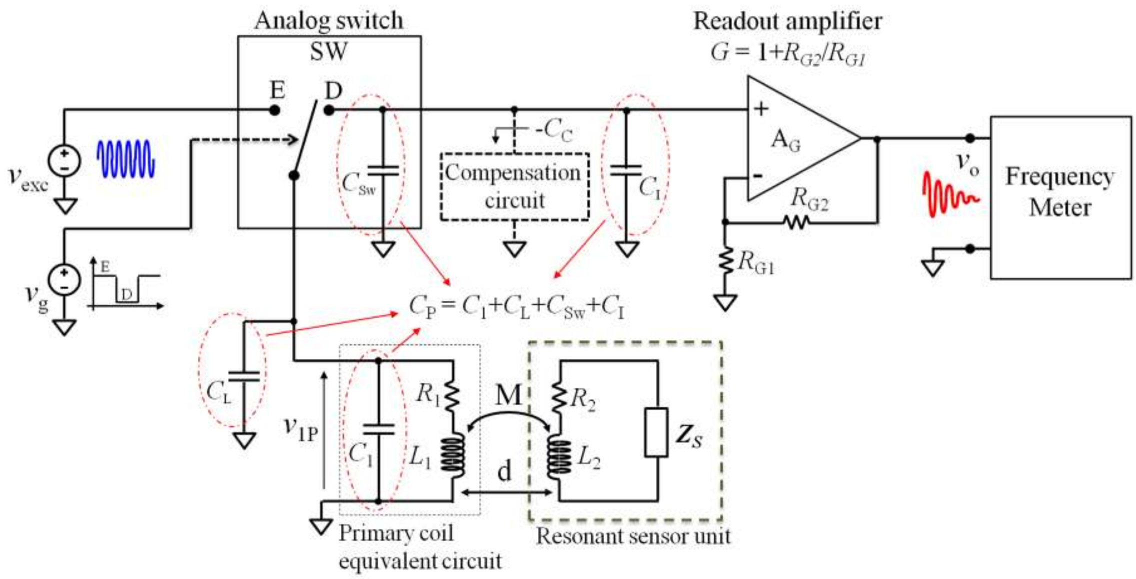

Figure 15. Block diagram of the interrogation system based on of time-gated technique with parasitic capacitance compensation circuit.

4.3. Parasitic Capacitance Compensation Circuit

Figure 16 shows the proposed capacitance compensation circuit. It is based on a high-bandwidth operational amplifier A_C operating as a negative impedance converter (NIC) to produce an effective negative capacitance $-C_C$. The voltage V_1 across CL_1 is applied across the reference capacitor C_A, thanks to the virtual short circuit at the input of A_C. The current I_{CA} through C_A is then amplified with gain $-R_{C2}/R_{C1}$, resulting in the current $I_1 = -j\omega C_A V_1(R_{C2}/R_{C1})$. The equivalent input impedance $Z_{Eq} = V_1/I_1$ is, therefore,

$$Z_{Eq} = \frac{V_1}{I_1} = \frac{V_1}{-\frac{j\omega C_A V_1 R_{C2}}{R_{C1}}} = -\frac{R_{C1}}{j\omega C_A R_{C2}} = \frac{1}{j\omega(-C_C)}. \tag{19}$$

Then, by taking C_A and R_{C1} as fixed, and making R_{C2} variable, the compensation circuit acts as an adjustable negative capacitance, given by

$$-C_C = -C_A \frac{R_{C2}}{R_{C1}}, \tag{20}$$

which can be tuned to compensate and possibly cancel C_P.

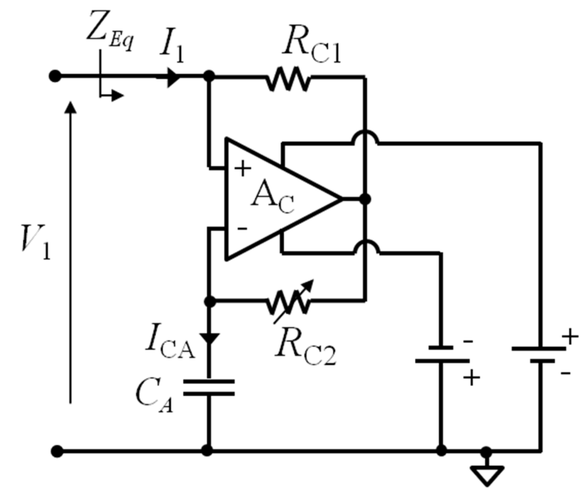

Figure 16. Schematic diagram of the parasitic capacitance compensation circuit.

5. Experimental Results and Discussion

5.1. Impedance Measurements with Coil-Coupled Capacitance Sensor and QCR

The experimental setup to test the system, according to the frequency-domain technique based on the block diagram of Figure 14, including the compensation circuit of Figure 16, is shown in Figure 17. The AD8045 (Analog Devices, Norwood, MA, USA) is used for the high-bandwidth operational amplifier A_C.

For the tests on the capacitance sensor configuration, the RSU is composed of a square planar spiral coil on Printed Circuit Board (PCB) with L_2 = 8.51 μH, R_2 = 3.2 Ω, and a reference capacitor C_S = 100 pF. According to Equation (1), the resulting resonant frequency and quality factor are f_S = 5.45 MHz and Q_S = 91, respectively. A PCB square planar spiral coil has also been used for the primary coil, with L_1 = 8.5 μH and R_1 = 5 Ω. A fixed capacitor C_F = 22 pF is connected in parallel to the primary coil, in order to set the parasitic capacitance and test the effectiveness of the compensation circuit.

The real part of the impedance Z_{1P} versus frequency has been measured at varying interrogation distance d, and hence the coupling factor k, for different values of the compensation capacitance C_C. The results are shown in Figure 18.

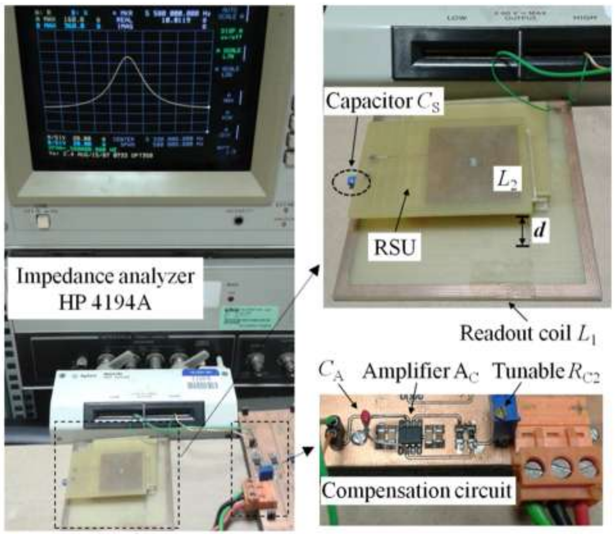

Figure 17. Experimental setup and interrogation system based on impedance-measurement technique with parasitic capacitance compensation.

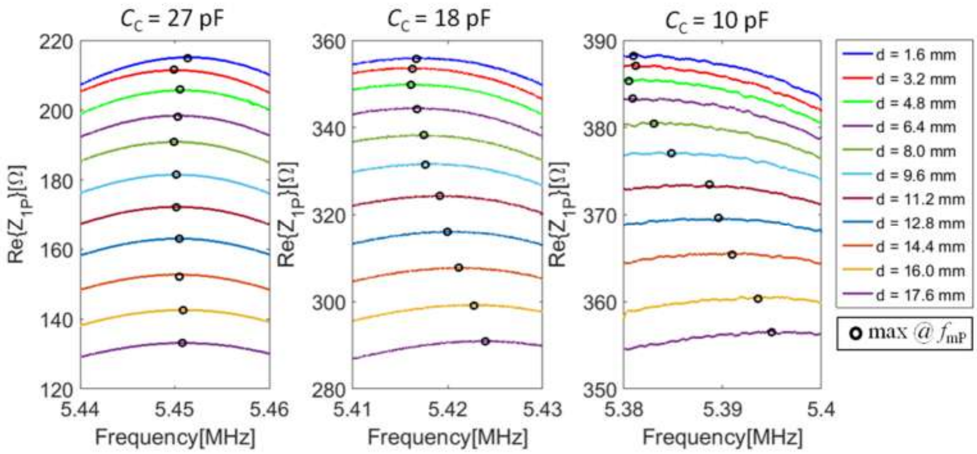

Figure 18. Measured maxima in Re{Z_{1P}} around f_S for different values of the compensation C_C, varying the distance d between CL_1 and the RSU. The frequency of the maxima at f_{mP} is highlighted with a black circle.

Figure 19 shows the measured frequency f_{mP} where the maximum of Re{Z_{1P}} near f_S occurs as a function of d, for different values of the compensation capacitance C_C. A monotonic decrease of k is expected by increasing d [29]. It can be observed that by increasing Cc, the expected undesired effect of the parasitic capacitances described in Section 3.3 decreases. With C_C = 27 pF, the value of f_{mP} becomes independent of d over the considered interrogation range of 16 mm, with a residual deviation of f_{mP} within 1 kHz, i.e., less than 200 ppm. The obtained value of Cc = 27 pF, slightly higher than the capacitor C_F = 22 pF, is ascribed to the presence of an extra capacitance of about 5 pF that concurs to form C_P. The results clearly demonstrate the effectiveness of the compensation technique and circuit.

Under ideal complete compensation condition, the measured f_{mP} approaches the unaffected value of f_m, discussed in Section 3.2, over the considered interrogation distance range. Then, for the considered RSU with a Qs = 91, a relative deviation $|f_{mP} - f_S|/f_S$ as low as 30 ppm is obtained from Equation (5).

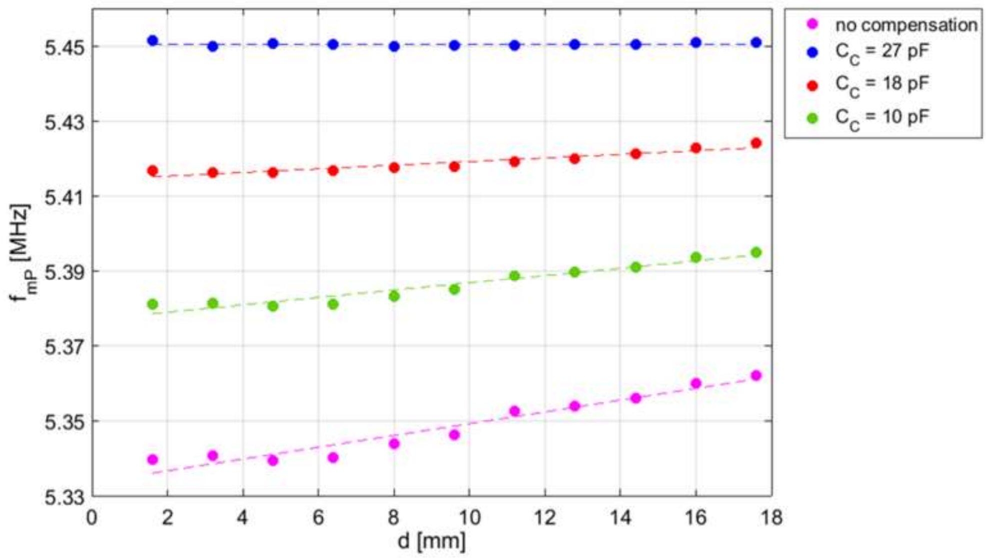

Figure 19. Measured frequency f_{mP} as a function of d for different values of C_C. The no compensation data are extrapolated from experimental values.

The same setup has been used for tests on coil-coupled electromechanical piezoelectric resonators. An AT-cut QCR with f_r = 4.432 MHz has been connected to CL_2. The parameters of the BVD equivalent circuit around fr of the adopted QCR are C_0 = 5.72 pF, R_r = 10.09 Ω, L_r = 77.98 mH, and Cr = 16.54 fF. The numerical analysis, discussed in Section 3.4, proves that parasitic capacitances in the order of tens of picofarads introduce negligible dependence of the measured resonant frequency on k. For this reason, the compensation circuit is not connected to the primary coil. Figure 20a shows the real part of the impedance Z_{1P}, measured in the frequency range around f_r for different values of the interrogation distance d. As it can be observed, while the magnitude of the maximum of Re{Z_{1P}} decreases by increasing d, the frequency f_{rP}, where the maximum occurs, shows residual variations as low as 1 Hz, i.e., less than 0.3 ppm, in the explored range of d, as shown in Figure 20b. This confirms the predicted independence of f_{rP} from d, and thus from k.

5.2. Time-Gated Measurements with Coil-Coupled Capacitance Sensor and QCR

Figure 21 shows the experimental setup used to test the interrogation system based on the time-gated technique shown in Figure 15. The excitation and gate signals $v_{exc}(t)$ and $v_g(t)$ are generated by two Agilent 3320A waveform generators (Agilent Technologies, Santa Clara, CA, USA). A tailored circuit comprising the analog switch SW (MAX393, Maxim Integrated, San Jose, CA, USA), the parasitic capacitance compensation circuit, and the readout amplifier A_G (OPA656, Texas Instruments, Dallas, TX, USA), has been developed. The readout output signal $v_O(t)$ has been connected to a high-resolution frequency meter Philips PM6680 (Philips International, Eindhoven, The Netherlands). The frequency meter is configured to perform measurements in a time window of duration T_M, starting after a delay time T_D from the beginning of the detection phase. The delay time T_D is used to skip the initial ringing in $v_O(t)$ [18,21]. The voltage $v_O(t)$ measured during detection phase, and the times T_D and T_M, are shown in Figure 22.

Firstly, tests have been done on the RSU with coil-coupled capacitance sensor, described in Section 5.1. The RSU has a PCB spiral coil with L_2 = 8.51 µH, R_2 = 3.2 Ω, and a capacitive sensor with C_S = 100 pF, resulting in a resonant frequency f_S = 5.45 MHz. The same PCB spiral coil described in Section 5.1, with L_1 = 8.5 µH and R_1 = 5 Ω, has been used as CL_1. The frequency of the excitation signal $v_{exc}(t)$ is set close to f_S to improve the transferred signal level.

Figure 23 reports the frequency f_{dP} of the damped sinusoid v_O(t) during the detection phase, measured at varying d for different values of the compensation capacitance C_C. A delay time T_D = 2 µs and a measurement time T_M = 6 µs have been chosen for all the measurements. As it can be observed, for the case of compensation of C_P, the dependence of f_{dP} on d is much reduced with respect to the cases with no or partial compensation. With $C_C \approx 48$ pF, f_{dP} has residual variations within 1.5 kHz, i.e., less than 300 ppm, across the explored interrogation range of about 17.6 mm.

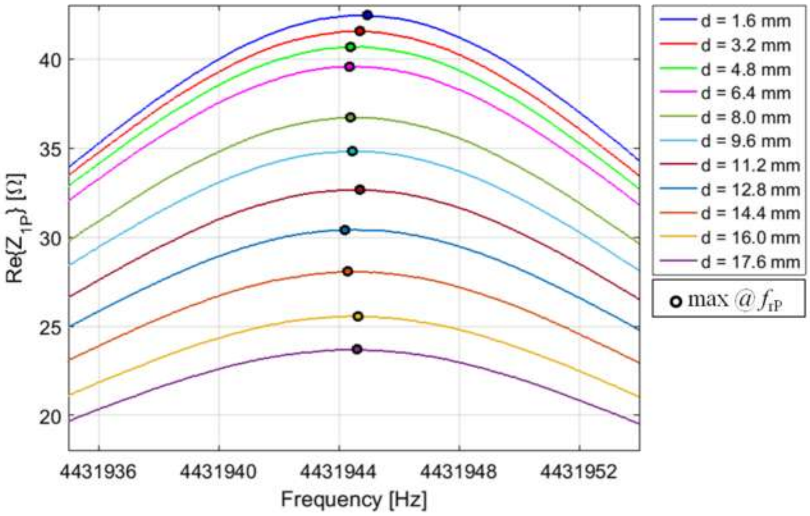

(**a**)

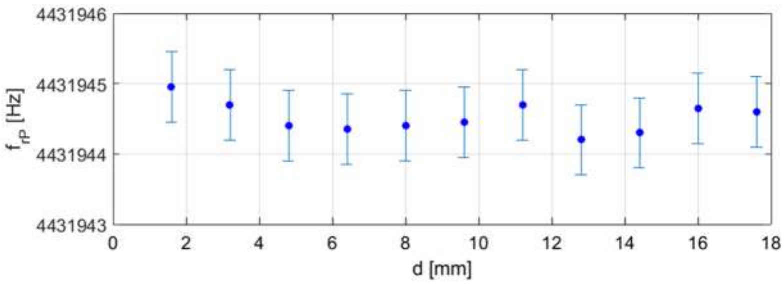

(**b**)

Figure 20. (**a**) Real part of Z_{1P} measured around the mechanical resonant frequency f_r of the quartz crystal resonator (QCR) connected to the primary coil CL_1 for different distances d. The frequency of the maxima at f_{rP} is highlighted with a black circle. (**b**) Frequency f_{rP} as a function of d. The error bars report the standard deviations calculated over 5 repeated measurements.

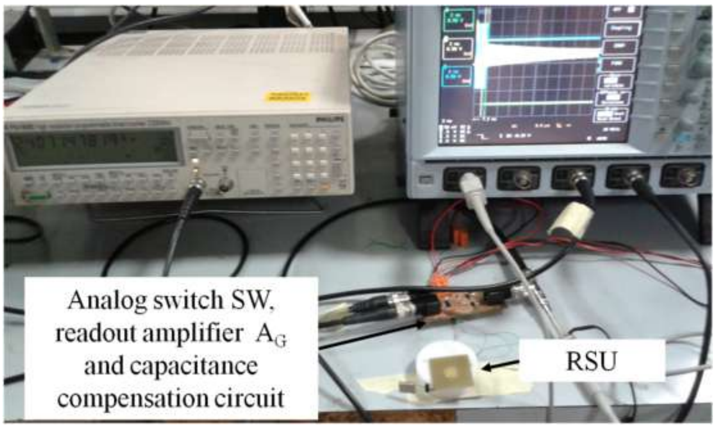

Figure 21. Picture of the experimental setup developed to implement the time-gated technique.

Under ideal complete compensation, the measured f_{dP} approaches the unaffected value of f_d discussed in Section 3.2. Then, for the considered RSU with Qs = 91, a relative deviation $|f_{dP} - f_S|/f_S$ as low as 15 ppm is obtained from Equation (8).

Then, tests have been run on an RSU made by a coil-coupled 4.432-MHz AT-cut QCR. The capacitance compensation circuit has been kept inactive, due to the predicted independence of f_{rP} from k for coil-coupled QCR. The frequency f_{rP} of the damped sinusoid $v_O(t)$ has been measured with varying the interrogation distance d.

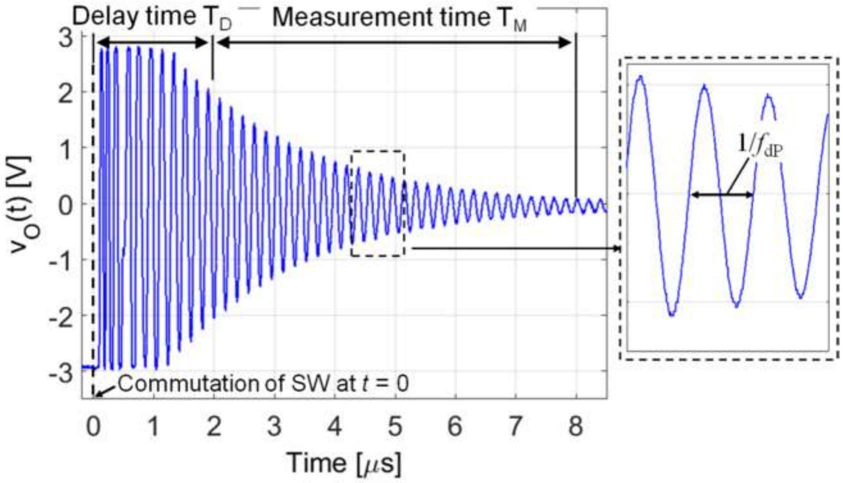

Figure 22. Measured output signal v_O(t) during the detection phase. Indications of the adopted delay time T_D and measurement time T_M are reported.

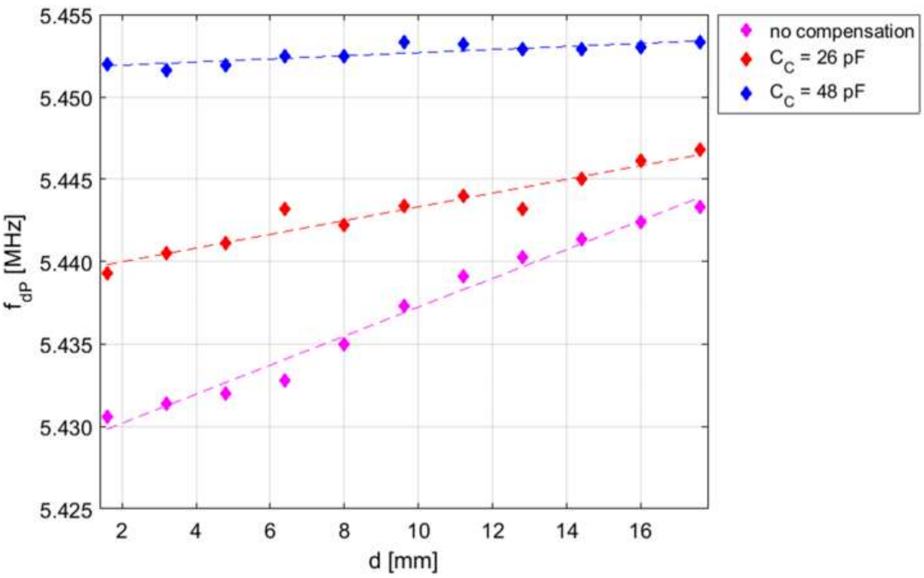

Figure 23. Frequency f_{dP} of the damped sinusoid $v_{1P}(t)$ measured as a function of the interrogation distance d for different values of the compensation capacitance C_C. A delay time T_D = 2 µs and a measurement time T_M = 6 µs have been set in the measurements.

Figure 24a shows the voltage $v_O(t)$ at the beginning of the detection phase for three different interrogation distances d. As it can be observed, the magnitude of $v_O(t)$ decreases with the increasing d, i.e., with decreasing k, while, as expected, the frequency f_{rP} is unaffected, as shown in Figure 24b. A residual variation of about 1.8 Hz, i.e., less than 0.5 ppm, has been obtained over the explored interrogation distance range of about 17.8 mm. In summary, the experimental results with coil-coupled

QCRs show that the total parasitic capacitance C_P estimated in about 48 pF, causes a negligible variation of the measured frequency f_{rP} over the explored interrogation range.

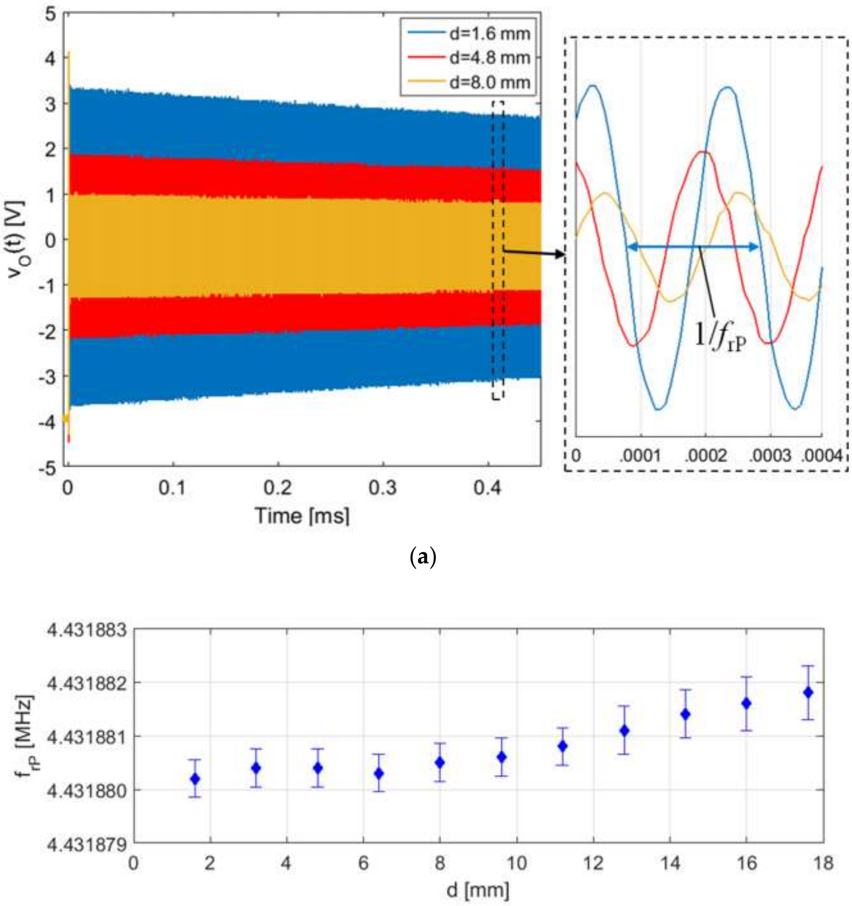

(**a**)

(**b**)

Figure 24. (**a**) Measured output signal $v_O(t)$ at the beginning of the detection phase for three different interrogation distances d. (**b**) Frequency f_{rP} as a function of d measured with a delay time T_D = 5 µs and a measurement time T_M = 10 ms. The error bars report the standard deviations calculated over 30 repeated measurements.

6. Conclusions

This work has investigated contactless interrogation techniques and readout circuits for passive sensors, exploiting the electromagnetic coupling between a primary and a secondary coil.

The sensor can be either a capacitive sensor or an electromechanical piezoelectric resonator. With both kinds of sensors, resonance can occur in the secondary circuit that can, therefore, be named resonant sensor unit (RSU). The interrogation of the RSU can be accomplished by techniques operating either in the frequency domain or in the time domain, which are ideally independent of the distance between the primary and secondary coils.

On the other hand, when unavoidable parasitic effects are considered, that combine in a lumped capacitance in parallel to the readout coil, an unwanted dependence of the readout frequency and quality factor on the interrogation distance is introduced, affecting similarly both the frequency- and time-domain techniques. Numerical analysis and experimental tests demonstrate that this dependence is detrimental on the accuracy of the readout frequency of the RSU. The inaccuracies are more relevant for the capacitive sensors, while for electromechanical piezoelectric resonators, the effect is negligible in most cases.

As a solution, an innovative approach has been proposed in which such parasitic capacitance is compensated by a purposely designed electronic circuit that has been prototyped and experimentally verified.

In tests carried out on a capacitive RSU with the proposed compensation circuit applied, a maximum deviation as low as 300 ppm on a resonant frequency of 5.45 MHz has been obtained over an interrogation range of almost 2 cm. This successfully demonstrates the validity of the proposed approach and circuit.

In addition, the experimental results have confirmed that the effect of the input parasitic capacitance is negligible when a coil-coupled piezoelectric quartz crystal resonator is used as the RSU.

Author Contributions: M.D. worked on the theory and modeling, and numerical analyses, contributed in the experimental activity, analysis of experimental data, and in writing the paper. M.B. contributed in the theory and modeling, experimental activity, analysis of experimental data, and in writing and revising the paper. M.F. contributed in the experimental activity, analysis of experimental data, and in revising the paper. V.F. coordinated the research and contributed in the theory and modeling, and in revising the paper.

Funding: This research received no external funding.

Conflicts of Interest: The authors declare no conflict of interest.

References

1. Ferrari, M.; Ferrari, V.; Guizzetti, M.; Marioli, D. An autonomous battery-less sensor module powered by piezoelectric energy harvesting with RF transmission of multiple measurement signals. *Smart Mater. Struct.* **2009**, *18*, 085023. [CrossRef]
2. Ferrari, M.; Ferrari, V.; Guizzetti, M.; Marioli, D.; Taroni, A. Piezoelectric multifrequency energy converter for power harvesting in autonomous microsystems. *Sensor Actuator A Phys.* **2008**, *142*, 329–335. [CrossRef]
3. Tan, Y.; Dong, Y.; Wang, X. Review of MEMS electromagnetic vibration energy harvester. *J. Microelectromech. Syst.* **2017**, *26*, 1–16. [CrossRef]
4. Dalola, S.; Ferrari, M.; Ferrari, V.; Guizzetti, M.; Marioli, D.; Taroni, A. Characterization of thermoelectric modules for powering autonomous sensors. *IEEE Trans. Instrum. Meas.* **2009**, *58*, 99–107. [CrossRef]
5. Cuadras, A.; Gasulla, M.; Ferrari, V. Thermal energy harvesting through pyroelectricity. *Sensor Actuator A Phys.* **2010**, *158*, 132–139. [CrossRef]
6. Dalola, S.; Faglia, G.; Comini, E.; Ferroni, M.; Soldano, C.; Zappa, D.; Ferrari, V.; Sberveglieri, G. Planar thermoelectric generator based on metal-oxide nanowires for powering autonomous microsystem. *Procedia Eng.* **2012**, *47*, 346–349. [CrossRef]
7. Demori, M.; Ferrari, M.; Bonzanini, A.; Poesio, P.; Ferrari, V. Autonomous sensors powered by energy harvesting by von karman vortices in airflow. *Sensors* **2017**, *17*, 2100. [CrossRef] [PubMed]
8. Sample, A.P.; Yeager, D.J.; Powledge, P.S.; Mamishev, A.V.; Smith, J.R. Design of an RFID-based battery-free programmable sensing platform. *IEEE Trans. Instrum. Meas.* **2008**, *57*, 2608–2615. [CrossRef]
9. Siddiqui, A.; Mahboob, M.R.; Islam, T. A passive wireless tag with digital readout unit for wide range humidity measurement. *IEEE Trans. Instrum. Meas.* **2017**, *66*, 1013–1020. [CrossRef]
10. Demori, M.; Baù, M.; Dalola, S.; Ferrari, M.; Ferrari, V. RFID powered system for contactless measurement of a resistive sensor array. In Proceedings of the 2018 IEEE International Instrumentation and Measurement Technology Conference (I2MTC), Houston, TX, USA, 14–17 May 2018.
11. Chatzandroulis, S.; Tsoukalas, D.; Neukomm, P.A. A miniature pressure system with a capacitive sensor and a passive telemetry link for use in implantable applications. *J. Microelectromech. Syst.* **2000**, *9*, 18–23. [CrossRef]
12. Rodriguez, S.; Ollmar, S.; Waqar, M.; Rusu, A. A batteryless sensor ASIC for implantable bio-impedance applications. *IEEE Trans. Biomed. Circuit Syst.* **2016**, *10*, 533–544. [CrossRef] [PubMed]
13. Bhamra, H.; Tsai, J.W.; Huang, Y.W.; Yuan, Q.; Shah, J.V.; Irazoqui, P. A subcubic millimeter wireless implantable intraocular pressure monitor microsystem. *IEEE Trans. Biomed. Circuit Syst.* **2017**, *11*, 1204–1215. [CrossRef] [PubMed]
14. Nopper, R.; Has, R.; Reindl, L. A wireless sensor readout system—Circuit concept, simulation, and accuracy. *IEEE Trans. Instrum. Meas.* **2011**, *60*, 2976–2983. [CrossRef]

15. Huang, Q.A.; Dong, L.; Wang, L.F. LC passive wireless sensors toward a wireless sensing platform: Status, prospects, and challenges. *J Microelectromech. Syst.* **2016**, *25*, 822–840. [CrossRef]
16. Babu, A.; George, B. A linear and high sensitive interfacing scheme for wireless passive LC sensors. *IEEE Sens. J.* **2016**, *16*, 8608–8616. [CrossRef]
17. Zhang, C.; Wang, L.F.; Huang, J.Q.; Huang, Q.A. An LC-type passive wireless humidity sensor system with portable telemetry unit. *J Microelectromech. Syst.* **2015**, *24*, 575–581. [CrossRef]
18. Demori, M.; Masud, M.; Baù, M.; Ferrari, M.; Ferrari, V. Passive LC sensor label with distance-independent contactless interrogation. In Proceedings of the 2017 IEEE Sensors Conference, Glasgow, UK, 30 October–1 November 2017.
19. Wang, X.; Larsson, O.; Platt, D.; Nordlinder, S.; Engquist, I.; Berggren, M.; Crispin, X. An all-printed wireless humidity sensor label. *Sensor Actuators B Chem.* **2012**, *166*, 556–561. [CrossRef]
20. Nopper, R.; Niekrawietz, R.; Reindl, L. Wireless readout of passive LC sensors. *IEEE Trans. Instrum. Meas.* **2010**, *59*, 2450–2457. [CrossRef]
21. Baù, M.; Ferrari, M.; Ferrari, V. Analysis and validation of contactless time-gated interrogation technique for quartz resonator sensors. *Sensors* **2017**, *17*, 1264. [CrossRef] [PubMed]
22. Ferrari, M.; Baù, M.; Tonoli, E.; Ferrari, V. Piezoelectric resonant sensors with contactless interrogation for mass sensitive and acoustic-load detection. *Sensors Actuators A Phys.* **2013**, *202*, 100–105. [CrossRef]
23. Demori, M.; Baù, M.; Ferrari, M.; Ferrari, V. Electronic technique and circuit topology for accurate distance-independent contactless readout of passive LC sensors. *AEU Int. J. Electron. Commun.* **2018**, *92*, 82–85. [CrossRef]
24. Morshed, B.I. Dual coil for remote probing of signals using resistive wireless analog passive sensors (rWAPS). In Proceedings of the 2016 United States National Committee of URSI National Radio Science Meeting, Boulder, CO, USA, 21 March 2016.
25. Yang, B.; Meng, F.; Dong, Y. A coil-coupled sensor for electrolyte solution conductivity measurement. In Proceedings of the 2013 2nd International Conference on Measurement, Information and Control, Harbin, China, 6 March 2014.
26. Arnau, A.; Ferrari, V.; Soares, D.; Perrot, H. Interface electronic systems for AT-Cut QCM sensors: A comprehensive review. In *Piezoelectric Transducers and Applications*, 2nd ed.; Springer-Verlag Berlin: Heidelberg, Germay, 2008; pp. 187–203.
27. DeHennis, A.; Wise, K.D. A double-sided single-chip wireless pressure sensor. In Proceedings of the MEMS 2002 IEEE International Conference, Las Vegas, NV, USA, 21–24 January 2002.
28. Harpster, T.J.; Hauvespre, S.; Dokmeci, M.R.; Najafi, K. A passive humidity monitoring system for in situ remote wireless testing of micropackages. *J Microelectromech. Syst.* **2002**, *11*, 61–67. [CrossRef]
29. Jacquemod, G.; Nowak, M.; Colinet, E.; Delorme, N.; Conseil, F. Novel architecture and algorithm for remote interrogation of battery-free sensors. *Sensor Actuators A Phys.* **2010**, *160*, 125–131. [CrossRef]